Advanced Functional Materials

ADVANCED FUNCTIONAL MATERIALS
www.afm-journal.de

RESEARCH ARTICLE OPEN ACCESS

Record Energy Storage Performance Metrics in Ferroelectric Hafnia-Based Films through Heterostructure Design

Ampattu R. Jayakrishnan[1,2] | Nuno Estrócio[1,2] | Inês Silva[1,2] | Raluca Negrea[3,4] | Marian C. Istrate[4] | Koppole C. Sekhar[5] | Luís Marques[1,2] | Judith L. MacManus-Driscoll[6] | Ignasi Fina[7] | Florencio Sánchez[7] | José P. B. Silva[1,2]

[1]Physics Center of Minho and Porto Universities (CF-UM-UP), University of Minho, Campus de Gualtar, Braga, Portugal | [2]Laboratory of Physics for Materials and Emergent Technologies, LapMET, University of Minho, Braga, Portugal | [3]Brunel Centre for Advanced Solidification Technology (BCAST), Brunel University London, Uxbridge, Middlesex, UK | [4]National Institute of Materials Physics, Magurele, Romania | [5]Department of Physics, School of Basic and Applied Science, Central University of Tamil Nadu, Thiruvarur, India | [6]Department of Materials Science & Metallurgy, University of Cambridge, Cambridge, UK | [7]Institut de Ciència de Materials de Barcelona (ICMAB-CSIC), Campus UAB, Barcelona, Spain

Correspondence: Ampattu R. Jayakrishnan (arjayakrishnan@fisica.uminho.pt) | José P. B. Silva (josesilva@fisica.uminho.pt)

Received: 24 February 2026 | **Revised:** 17 March 2026 | **Accepted:** 24 March 2026

Keywords: energy storage | ferroelectric HfO_2 | heterostructures | relaxor ferroelectrics

ABSTRACT

Capacitive energy storage is part of a promising energy harvesting and storage solution to power Internet of Things (IoT) sensors, overcoming the critical limitations of conventional supercapacitors and micro-batteries. Moreover, achieving high recoverable energy storage density (*ESD*) and high efficiency (η) simultaneously is a key goal in energy storage, often requiring hybrid systems (e.g., combining batteries and supercapacitors) to balance the trade-offs. Here, we demonstrate a ultra-thin film capacitor with unprecedented high *ESD* that can be efficiently released at low operating voltage. This is achieved by using a novel heterostructure design combining ferroelectric La-doped HfO_2 and a ferroelectric perovskite that is a relaxor induced by polar nanoregions, which enables a low hysteresis loss in the capacitor, thereby leading to an improved η. Additionally, the relaxor ferroelectric layer thickness was optimized to give an optimum voltage drop to allow high maximum polarization and low remnant polarization, the former to allow an *ESD* of over 50 J/cm^3, and the latter to allow η to be maximized at ~95%. Therefore, our fluorite/perovskite heterostructure design and unique materials strategy have *together* provided a novel way to achieve unprecedented dielectric energy storage properties, proving a new route to electrostatic energy storage for autonomous IoT sensors.

1 | Introduction

The Internet of Things (IoT) refers to a network of devices that can sense, communicate, and act without human intervention, transforming traditional systems into intelligent ones. This interconnected network of smart devices has fostered a more efficient, automated, and responsive world. So far, it has transformed our healthcare, automotive, and agriculture industry [1]. In addition, artificial intelligence (AI) introduces a new paradigm in how sensors collect, interpret, and act on data, with co-design and benchmarking key to their success [2].

However, modern IoT sensor nodes typically rely on rechargeable lithium (Li)-ion batteries [1]. The Li-ion batteries have become the dominant electrochemical energy storage technology due to their high energy density and well-developed manufacturing

infrastructure [3, 4]. Despite their technological maturity, fundamental scientific challenges still limit further improvements in performance, safety, and durability [3].

Moreover, modern IoT sensor nodes typically rely on standard 3000 mAh lithium-ion batteries, which offer a lifetime of no more than 2 years (approximately 2000 charge–discharge cycles) [1, 5]. Consequently, battery failure or replacement disrupts the continuous operation of the IoT sensors. Another concern is the growing dependence on materials that are increasingly scarce and toxic, particularly lithium (Li). Global Li production is about 100 000 tons per year, and the International Energy Agency (IEA) anticipates this demand to increase to 240 000–450 000 tons by 2030 [6]. To circumvent this major problem, current research is shifting toward compact autonomous IoT nodes capable of powering the electronics behind sensors through an integrated energy harvesting-energy storage strategy [1]. In particular, the harvest-storage architecture that can power the electronics coupled to self-powered sensors (operating via phenomena such as triboelectric, piezotronics, or pyro-phototronic effects [7–9], mitigates limitations associated with the batteries. Therefore, investigation of alternative complementary technologies is essential for the more extended implementation of IoT sensors. For this purpose, electrochemical supercapacitors and electrostatic dielectric capacitors are considered promising solutions [10–13]. Commercial electrochemical capacitors suffer from low energy storage density (<30 J/cm^3) and limited cycling stability ($\leq 10^5$ cycles) [10]. In addition, they face the challenges of compatibility with complementary metal-oxide-semiconductor (CMOS) for on-chip integration and reducing device size (electrochemical capacitors are around 1 μm or thicker), restricting broader applicability [11–13]. Electrostatic dielectric capacitors, on the other hand, offer smaller size, superior energy storage density, high efficiency, and long cycling life, and they can enable perpetual IoT sensor operation.

Recently, dielectric capacitors are attracting significant attention for ES applications [14, 15]. The ES performance of a dielectric capacitor is determined by using the polarization-electric field (*P-E)* loops, and the parameters used to establish the performance matrices are recoverable energy storage density (*ESD*), efficiency (η), and applied electric field (E). These parameters are determined using the following equations [14, 15]:

$$W_{\text{stored}} = \int_0^{P_{\text{m}}} E \, dP \tag{1}$$

$$ESD = \int_{P_{\text{r}}}^{P_{\text{m}}} E \, dP \tag{2}$$

$$\eta = \frac{ESD}{W_{\text{stored}}} \tag{3}$$

here, W_{stored} is the total energy density, P_m is the maximum polarization, and P_r is the remnant polarization. Therefore, the high ES performance of a dielectric capacitor is shaped by the combination of a large P_m and a small P_r, at a certain E.

Among different dielectric materials, perovskite-structure oxide-based relaxor ferroelectrics (RFEs) and anti-ferroelectrics (AFEs) stand out for their superior *ESD* and η, surpassing those of conventional ferroelectrics (FEs) and linear dielectrics [14, 15]. The notable works on top-performing AFE and RFE- based perovskite oxides possess larger *ESD* (>150 J/cm^3) and η (> 90%), although they require high operating voltages (>100 V) [16, 17]. However, the reliable and safe operation of IoT sensors demand high-quality dielectric capacitors with superior ES performance at low applied voltages, comparable to micro-batteries (most common supply voltage is in the range 1.8–5 V) [18]. Therefore, fabricating a dielectric capacitor with excellent ES performance at low voltages is essential [19].

The discovery of ferroelectricity (FE) and AFE in sub-10 nm $Hf_xZr_{1-x}O_2$ (HZO)-thin films has attracted interest for the development of ES dielectric capacitors due to their high P_m achieved at low voltages [20]. Furthermore, there are works reporting high ES using HZO-based dielectric capacitors [21–23]. An AFE HZO 3D capacitor incorporating Al_2O_3 insulation layer via superlattice engineering reported a large *ESD* ~ 81 J/cm^3 and an η ~ 73% at a high applied voltage of ~40 V [21]. Another work exploited the formation of polar nanoregions (PNRs) in Al doped AFE HfO_2 capacitors and achieved an *ESD* ~ 100 J/cm^3 with an η < 85%, at ~9 V [22]. However, detailed studies on the observed good performance using this approximation have not been done to further optimize ES parameters. More recently, an Al_2O_3 inserted HfO_2 capacitor reported a large *ESD* ~ 130 J/cm^3 and an η ~ 80% in, with a lower applied voltage of ~7.5 V [23]. Even though the *ESD* is similar to that achieved in perovskite AFE and RFE-based capacitors, the efficiency remains limited, not exceeding 85%.

Considering the shortcomings of the aforementioned works of having both high *ESD* and high η in the same capacitor, the development of a highly efficient, eco-friendly dielectric capacitor material capable of delivering superior ES performance at low voltages is imperative for IoT sensors. With this challenge in mind, in this work a FE/RFE heterostructure capacitor was designed to leverage the unique properties of two layers of high P_m at low voltage and RFE behavior for high efficiency. The materials chosen for these two layers are FE La (5 cat.%)- doped HfO_2 (La:HfO_2) and RFE (the latter selected owing to its weakly coupled polar nanoregions (PNRs), which enable potentially high η) Pb-free $0.85[0.6Ba(Zr_{0.2}Ti_{0.8})O_3$–$0.4(Ba_{0.7}Ca_{0.3})TiO_3]$–$0.15SrTiO_3$ (BCZT–STO) [24], respectively.

In order to optimize the voltage drop across the film stack to achieve switching at the voltage where P_m achieves its maximum value, we tuned the BCZT-STO layer thickness and then probed the FE and ES performance. This enabled us to achieve an excellent balance between *ESD* and η at a low voltage. A comprehensive analysis elucidating the underlying physical mechanisms by which the RFE introduction enhances the ES performance of La:HfO_2-based dielectric capacitors under low-voltages was also undertaken.

2 | Experimental Section

Bilayered heterostructures combining La:HfO_2 (with a thickness of 10 nm) and BCZT-STO (with different thicknesses of 0, 5, 50, 100, and 200 nm) were grown by PLD on LSMO-buffered

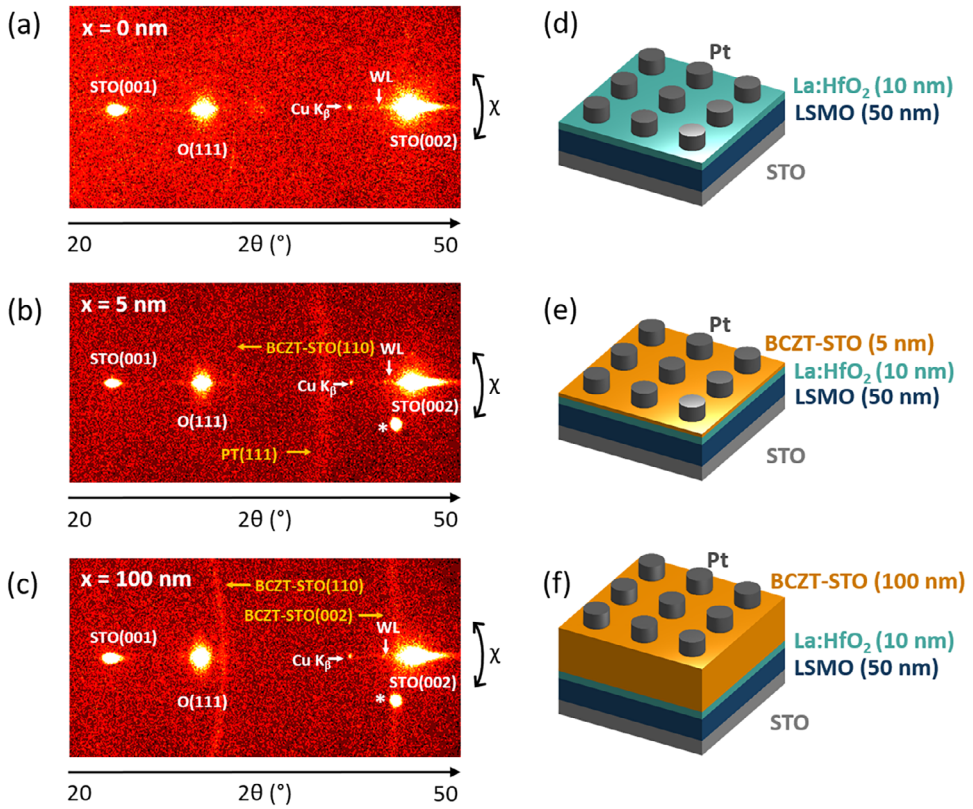

FIGURE 1 | 2θ-χ XRD maps of the STO/LSMO/La:HfO_2/BCZT-STO/Pt samples with BCZT-STO thicknesses of (a) 0 nm, (b) 5 nm, and (c) 100 nm, respectively. The circular spot marked with an asterisk that appears in some of the 2θ-χ maps is an artifact caused by the 2D detector. The weak peaks near 41.7° and 44.4° are STO(002) reflections caused by the K_β line of Cu ($\lambda = 1.391$ Å) and the L line of W ($\lambda = 1.476$ Å), respectively [34]. (d–f) show sketches of the thin film device structure corresponding to each XRD map.

STO(001) substrates. The growth parameters for LSMO, La:HfO_2, and BCZT-STO layer are given in ref [24–26]. After BCZT-STO layer growth, in order to sufficiently oxidize the films, they were annealed for 20 min at 775°C under 0.1 mbar of O_2 [24]. For the electrical characterization, top Pt electrodes (3.14×10^{-4} mm^2 and 20 nm thick) were deposited through stencil masks by DC magnetron sputtering. As a result, a metal-ferroelectric-relaxor ferroelectric-metal structure, LSMO/La:HfO_2/BCZT-STO/Pt is fabricated. Platinum is considered a chemically inert electrode used to study the ferroelectric properties of HfO_2-based films because it does not act as an oxygen scavenging layer, unlike the conventionally used TiN electrodes [27, 28].

The crystal structure was analyzed by X-ray diffraction (XRD) with Cu Kα radiation using a Bruker D8-Advance diffractometers equipped with 2D detector [29]. For microstructural characterization, cross-sectional specimens were prepared using standard methods involving cutting and polishing, followed by ion milling using a precision ion polishing system (PIPS). Atomic-resolution high-angle annular dark-field scanning transmission electron microscopy (HAADF-STEM) imaging and energy-dispersive X-ray spectroscopy (EDS) mapping were carried out using a probe-corrected SPECTRA 300 TEM (Thermo Fisher Scientific), equipped with a Super-X EDS detector and operated at 200 kV. A convergence semi-angle of 15.7 mrad was used, yielding a depth of focus of approximately 10 nm, which optimized EDS signal acquisition. A camera length of 91 mm was employed, corresponding to HAADF detector collection angles in the range of 72–200 mrad. Experimental HAADF-STEM images were further analyzed using atomic structure models performed with CrystalKit software (Total Resolution LLC).

Ferroelectric characterization was performed at room temperature by measuring the polarization–voltage (P–V) loops, with the LSMO electrode grounded and the Pt electrode biased at 1 kHz using the AixACCT TFAnalyser3000 system. The leakage contribution was compensated using the standard dynamic leakage current compensation (DLCC) method [30, 31]. For the ES performance evaluation, the electric field was estimated by using the applied voltage divided by the total FE/RFE heterostructure thicknesses.

3 | Results and Discussion

Figure 1a–c displays the XRD 2θ-χ maps of the STO/LSMO/La:HfO_2/BCZT-STO/Pt samples, with corresponding BCZT–STO layer thicknesses of 0, 10, and 100 nm, respectively, while Figure 1d–f shows the sketches of the corresponding samples for each map, respectively. The intense spots at $\chi = 0°$ and 2θ–23° and 2θ–46° depict the STO(001) and STO(002) reflection, with the corresponding LSMO spots overlapped. All samples show a Bragg spot at $\chi = 0°$ and 2θ–30°, confirming the orthorhombic (o) La:HfO_2 (111) reflection [29, 32]. The Bragg spot has a circular shape, in agreement with the epitaxial growth of La:HfO_2 layer on LSMO/STO(001) [32]. A low intensity

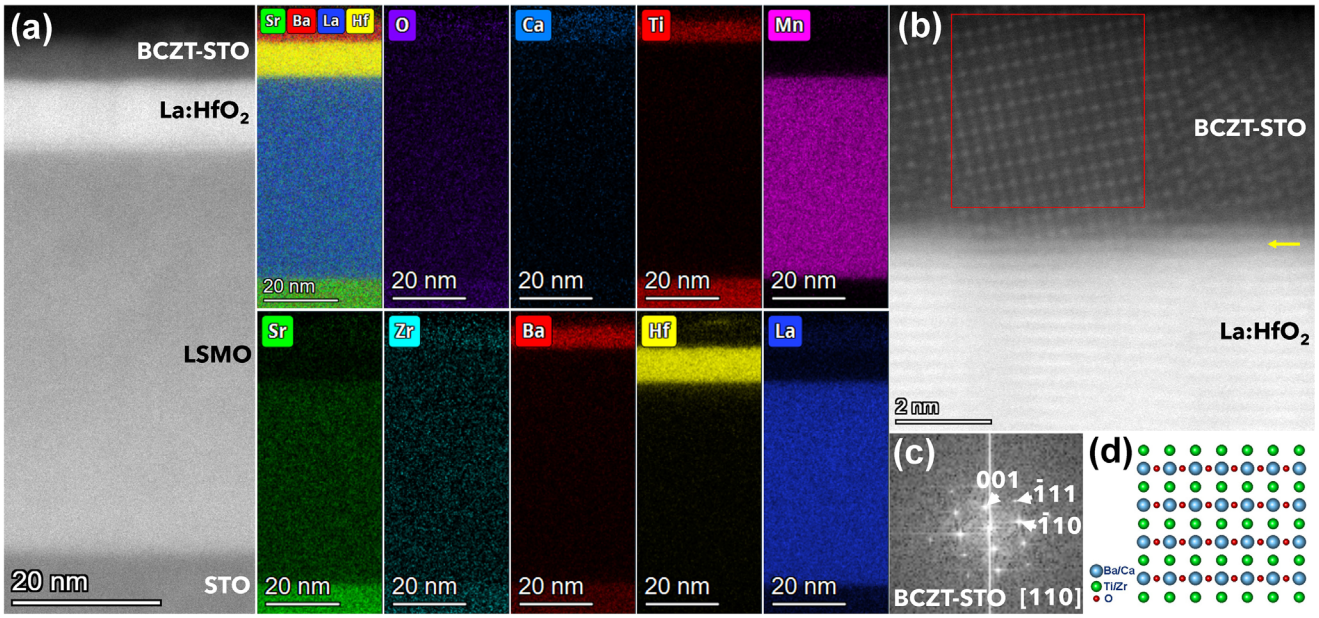

FIGURE 2 | (a) HAADF–STEM image and corresponding EDS elemental maps of the STO/LSMO/La:HfO_2/BCZT-STO/Pt heterostructure (5 nm thick BCZT-STO) (b) atomic-resolution STEM image around the La:HfO_2/BCZT-STO interface (marked with a yellow arrow), (c) FFT corresponding to the red box in (b), indexed to the perovskite BCZT structure along the [110] zone axis, and (d) atomic arrangement of the perovskite BCZT-STO along the [110] zone axis, where Ba/Ca, Ti/Zr, and O atomic columns are indicated.

arc-shaped spot is observed at 2θ–32° in Figure 1b, corresponding to the (110) reflection from the BCZT-STO layer [28]. The low intensity is a consequence of the low thickness (5 nm) of the BCZT layer. Additionally, the arc shaped spot at 2θ–40° corresponds to the (111) reflection of the Pt electrode. The map of the sample with the thickest film (100 nm) shown in Figure 3c also exhibits arc-shaped reflections at 2θ–32° and 2θ–45°, corresponding to (110) and (002) reflections of BCZT [24, 33]. The arc-shape along χ indicates the polycrystallinity of the BCZT-STO layer irrespective of its thickness. In addition, regarding the possible effect of the BCZT-STO layer on the La:HfO_2 thin film crystallization behavior, XRD measurements in all the samples demonstrate that there is no *o*-(111) La:HfO_2 peak change, confirming that this possible effect is negligible.

Microstructural characterization of the sample with the 5 nm thick BCZT-STO layer, corresponding to the sketch shown in Figure 1e, was undertaken by STEM. The cross-section HAADF–STEM image in Figure 2a shows the STO substrate, and the LSMO (50 nm), La:HfO_2 (10 nm), and BCZT-STO (5 nm) layers. The elemental mapping images at the right, corresponding to O, Sr, Ba, Ca, Zr, Ti, and Mn, confirms the sharp interfaces between BCZT-STO, La:HfO_2, LSMO, and STO(001), with negligible interdiffusion. A more detailed analysis is given in Supporting Information (Figure S1). Figure S2 shows that the La:HfO_2 layer in the STO/LSMO/La:HfO_2/BCZT-STO/Pt sample (Figure 1e) exhibits well-defined atomic columns, demonstrating a high degree of crystallinity of the La:HfO_2 layer. Two representative regions within the film (labeled 1 and 2 in Figure S2) were selected for local structural analysis. The Fast Fourier Transform (FFT) patterns extracted from these regions are indexed to the *o*-phase of La:HfO_2, confirming the stabilization of the non-centrosymmetric *o*-phase structure within the film. The FFT from region 1 can be indexed along the [-211] zone axis, with characteristic reflections corresponding to the {111}, {113}, and {022} planes. In contrast, the FFT from region 2 is indexed along the [101] zone axis, showing prominent {111} and {020} reflections. The presence of these reflections is consistent with *o*-phase symmetry [35]. The observation of different zone axes within closely spaced regions signals, the existence of the crystal variants, which is a consequence of the different {111} orientations of La:HfO_2 on LSMO(001) [36]. To analyze the crystallographic symmetry of the BCZT layer, a FFT pattern was extracted from the region highlighted with a red square in Figure 2b. The FFT can be indexed along the [110] zone axis of the perovskite BCZT structure, with clearly resolved reflections corresponding to the (001), (−111), and (−110) planes (Figure 2c). These reflections are consistent with the expected perovskite structure of BCZT. The experimental atomic-resolution HAADF-STEM images are also in perfect agreement with the projected atomic model along the [110] zone axis of the perovskite structure (space group: P4mm (99) and a = b = 4.092 Å, c = 4.099 Å, $\alpha = \beta = \gamma = 90°$), shown in Figure 2d, where Ba/Ca occupy the A-site positions, Ti/Zr the B-site positions, and oxygen atoms form the corner-sharing octahedral framework. Overall, the combined real-space imaging and reciprocal-space analysis demonstrates that the BCZT-STO layer in the STO/LSMO/La:HfO_2/BCZT-STO/Pt film (Figure 1e) is structurally coherent, with a well-ordered crystallographic arrangement within the FE/RFE heterostructure.

Figure 3a displays the *P-V* loops measured for the LSMO/La:HfO_2/BCZT-STO/Pt dielectric capacitors, at an applied voltage of 6.5 V. The *P-V* loop shown in Figure S3a of the LSMO/La:HfO_2/Pt confirms its FE nature. The P_r value for a single La:HfO_2 film is 16 μC/cm^2, in agreement with previous reports [25, 26].

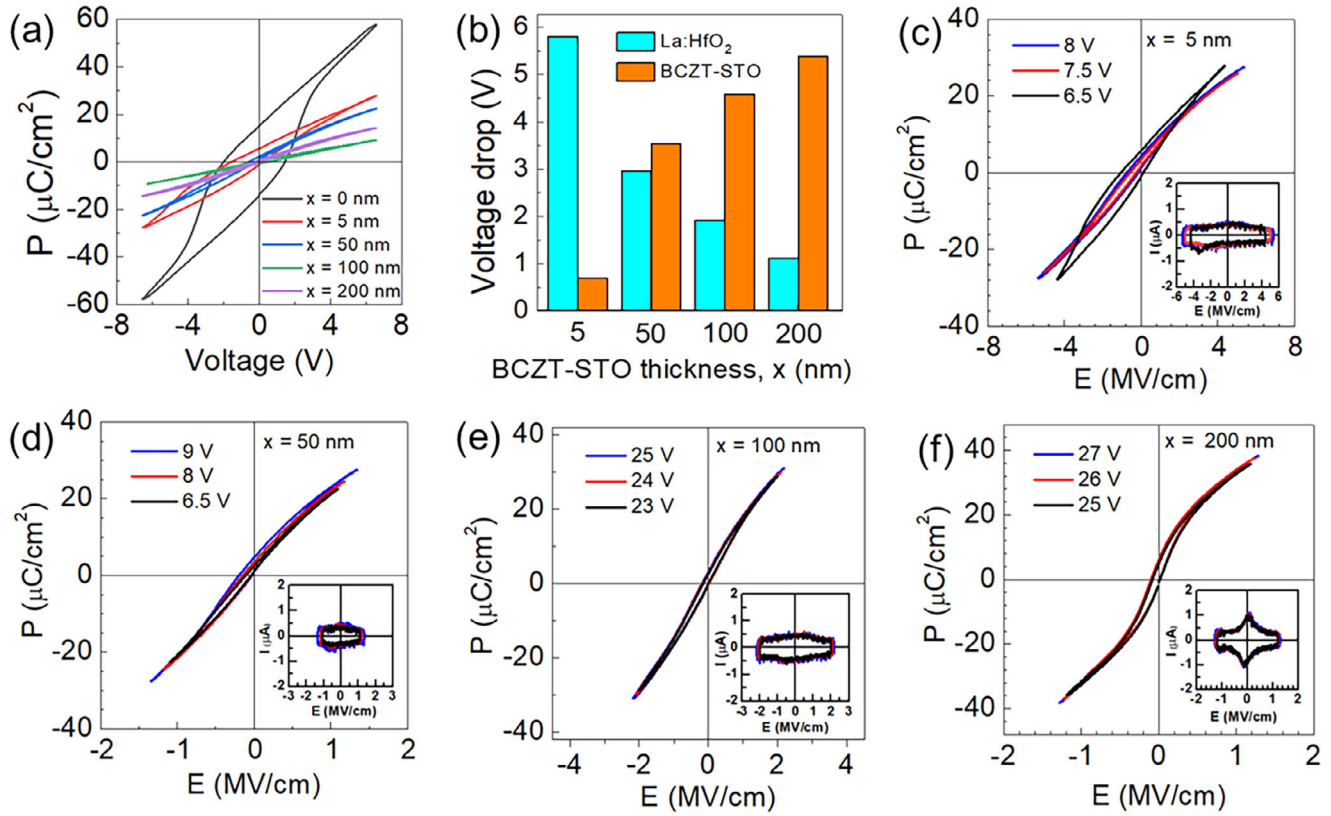

FIGURE 3 | (a) *P-V* loops for different BCZT-STO layer thicknesses (x) in LSMO/La:HfO_2/BCZT-STO/Pt at a constant voltage of 6.5 V, (b) calculated voltage drop across the La:HfO_2 and BCZT-STO layers as a function BCZT-STO layer thickness (x). *P-E* loop at different voltages for different BCZT-STO layer thicknesses, x. (c) x = 5 nm, (d) x = 50 nm, (e) x = 100 nm, and (f) x = 200 nm, respectively. The voltage values noted within the plots of (c)-(f) correspond to the voltage drop across the La:HfO_2/BCZT-STO layers.

Figure 3a probes the role of the BCZT-STO layer thickness in combination with a La:HfO_2 layer, i.e., in studies of LSMO/La:HfO_2/BCZT-STO (x nm)/Pt, where x ranges from 0 to 200 nm. It is found that the increasing presence of BCZT-STO (higher x) leads to a decrease in the P_m and P_r values, making the hysteresis loops slimmer when compared to the *P-V* response of the LSMO/La:HfO_2/Pt. This slim nature of the *P-V* loops, as well as the monotonous decrease in the P_m and P_r with increasing RFE layer thickness is attributed to the decreasing (increasing) calculated voltage drop across the FE La:HfO_2 (RFE BCZT-STO) layers with increasing x, as shown in Figure 3b. The reason for this inverse relation in voltage drop is discussed later.

To explore the effect of the BCZT-STO layer on the FE response of the capacitors, we have studied *P-E* loops as a function of applied electric field for LSMO/La:HfO_2/BCZT-STO/Pt. The *P-E* loops for the LSMO/La:HfO_2/BCZT-STO/Pt samples for BCZT–STO layer thicknesses, x, of 5, 50, 100, and 200 nm show different *P-E* loops (Figure 3c–f). The measured *V* drop values across the BCZT-STO layers in each film stack are noted in each plot, while the insets of the same figures show their corresponding *I-E* curves. Mixed FE/RFE behavior is observed for 5, 50, and 100 nm, whereas a RFE response is observed for 200 nm. The breakdown electric field/voltage increases with increasing the BCZT-STO thickness, x, because of the different voltage drops across the La:HfO_2 and BCZT-STO layers (Figure S4). It is noted that the voltage across the La:HfO_2 layer is always below 8 V (Figure S4), which prevents it from breaking down.

For the 5 nm BCZT–STO, most of the voltage drop (7.85 V) occurs in the La:HfO_2 layer, but there is still some voltage drop (0.85 V) across the BCZT–STO, for an applied voltage of 8 V, to cause mixed FE/RFE behavior. There could also be an interfacial proximity effect, as observed for Sm-doped $Hf_{0.5}Zr_{0.5}O_2/Hf_{0.5}Zr_{0.5}O_2$ [35] and $Al_{0.8}Sc_{0.2}N$/AlN [37] heterostructures, to enable switching of the BCZT-STO layer at lower applied voltages. This effect would also produce a mixed FE/RFE behavior.

For the 50 and 100 nm BCZT–STO layers, the voltage drop across the BCZT-STO layer starts to become dominant (Figure S4c–e), thereby producing still a mixed FE/RFE behavior. This hypothesis is supported by the *I-E* curves shown in the inset of Figure 3c–e, which show broad peaks related to the mixed FE/RFE behavior for the 5, 50, and 100 nm BCZT–STO layer. By further increasing the thickness of the BCZT-STO layer to 200 nm, the voltage drops across the La:HfO_2 layer become negligible compared to the voltage drop across the BCZT-STO layer. Here, the higher V drop across the BCZT-STO gives rise to a typical RFE behavior, corroborated by the *I-E* curves in the inset of Figure 3f that show sharp switching current peaks at around $E \sim 0$ MV/cm along with a very slim *P-E* loop, ascribed to the RFE characteristics [38, 39].

Next, we evaluate the ES characteristics of the different, i.e., *ESD* and η based on their *P-E* loops and using Equations (2) and (3). Figure 4a displays the *ESD* as a function of the applied voltages for the LSMO/La:HfO_2/BCZT-STO/Pt, with thickness ranging from 5

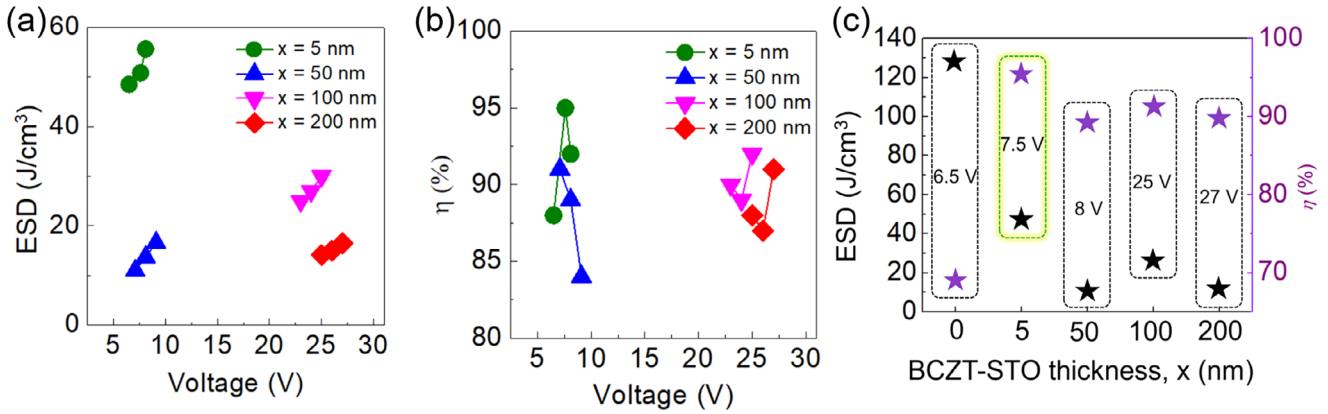

FIGURE 4 | (a) *ESD* and (b) η for the LSMO/La:HfO_2/BCZT-STO/Pt as a function of voltages, (c) best values of *ESD* and η as a function of BCZT-STO layer thickness. The optimum applied voltage values for each thickness are shown inside the figure.

to 200 nm. As expected, the *ESD* value increases with the applied voltage for all the capacitors. For capacitors containing BCZT-STO, the *ESD* is found to be higher for the lowest layer thickness of 5 nm because of the higher applied electric field. On the other hand, the *ESD* value is lower for the LSMO/La:HfO_2/BCZT-STO/Pt capacitor compared to the LSMO/La:HfO_2/Pt capacitor (*ESD* = 133 J/cm^3 and η = 68%) because P_m is reduced when the BCZT-STO RFE is present.

Figure 4b shows η as a function of the applied voltage, for the different LSMO/La:HfO_2/BCZT-STO/Pt. Remarkably, the η values are much higher compared to the LSMO/La:HfO_2/Pt (η = 68%), where no BCZT-STO layer is present. This is understood based on the FE/RFE mixed behavior when both La:HfO_2 and BCZT-STO layers are present. η is as high as 95% in the LSMO/La:HfO_2/BCZT-STO/Pt for the 5 nm BCZT-STO layer thickness at an applied voltage of 7.5 V (Figure 4b). This is a remarkable result since most of the HZO based capacitors exhibit η *b*elow 85% for applied voltages < 10 V [21–23, 40–45]. The high value is explained by both a high P_m value being obtained from the switching of the La:HfO_2 layer and also the very slim loop obtained from the switching of the relaxor BCZT-STO layer. This is analysed in more detail later. The fact that BCZT-STO dominates the loop shape over the La:HfO_2 is indicative again of a proximity effect between the layers [35, 37]. Figure 4c shows *ESD*/η versus BCZT-STO layer thickness with optimum applied voltage shown in the plot for the different thicknesses. The 5 nm BCZT-STO layer thickness shows the best combination of *ESD* (51 J/cm^3) and η (95%), achieved at an applied voltage of only 7.5 V.

Now we turn to understanding the ES performance values of the FE/RFE heterostructures by considering the voltage drop across them (for a total applied voltage of 6.5 V (Figure 3b). The FE La:HfO_2 layer and the RFE BCZT-STO layer act as two capacitors in series [46]. Thus, the total applied voltage (V) is distributed between the two layers as follows:

$$V = V_{\mathrm{FE}} + V_{RFE} \tag{4}$$

where V_{FE} and V_{RFE} represent the voltages across the La:HfO_2 and BCZT-STO layers, respectively. It should be noted that the expression for V_{FE} and V_{RFE} in the case of an ideal parallel plate capacitor is given as follows [46]:

$$V_{\mathrm{FE}} = \left(\frac{\varepsilon_{\mathrm{FE}}}{t_{\mathrm{FE}}} \cdot \frac{t_{RFE}}{\varepsilon_{RFE}} + 1\right)^{-1} V \tag{5}$$

and

$$V_{RFE} = \left(\frac{\varepsilon_{RFE}}{t_{RFE}} \cdot \frac{t_{\mathrm{FE}}}{\varepsilon_{\mathrm{FE}}} + 1\right)^{-1} V \tag{6}$$

where ε_{FE}, ε_{RFE}, t_{FE}, and t_{RFE} represent the dielectric constants of La:HfO_2 (ε_{FE} = 30) [47], and BCZT-STO (ε_{RFE} = 125) [22], and the thickness of La:HfO_2 and BCZT-STO layers, respectively. Here, the t_{FE} is constant, while t_{RFE} is the variable. As per Equations (5) and (6), and as shown in Figure 3b, the increase in t_{RFE} causes a reduction in V_{FE} and consequently an increase in V_{RFE}. Since the P_m and P_r values for the LSMO/La:HfO_2/Pt are higher than the ones observed in the LSMO/BCZT-STO/Pt with a BCZT-STO layer thickness of 200 nm (Figure S3b), the inclusion of the BCZT-STO layer in the capacitor causes a decrease in the P_m and P_r values. Interestingly, an improvement in the P_m and P_r values was observed when the BCZT-STO layer thickness increased from 100 to 200 nm, consistent with reports on other perovskite systems where polarization increases with film thickness. Thus, larger thicknesses hinder depolarizing fields and interfacial dead layers, enabling the domains to grow and align more effectively [48, 49].

The physical mechanism behind the ES performance enhancement in the FE/RFE heterostructures is schematically shown in Figure 5 and can be understood as follows. The FE LSMO/La:HfO_2/Pt provides a large P_m and a moderate P_r attributed to the presence of the switchable macrodomains (shown in the insets of Figure 5a) and thereby, constituting a larger *ESD* (Figure 5a). On the other hand, the RFE LSMO/BCZT-STO/Pt exhibits a pinched *P-E* loop due to the presence of switchable PNRs that cause a reduced P_r and also, ultrahigh η from the PNRs (Figure 5b) [14, 24]. The LSMO/La:HfO_2/BCZT-STO/Pt with x = 5 nm has an optimized voltage drop across the La:HfO_2 FE and BCZT-STO RFE layers (i.e. high across the La:HfO_2 and low across the BCZT-STO). This allows for a high P_m from the La:HfO_2 and a low P_r from the BCZT-STO, caused by interaction (proximity effect) between the macrodomains in

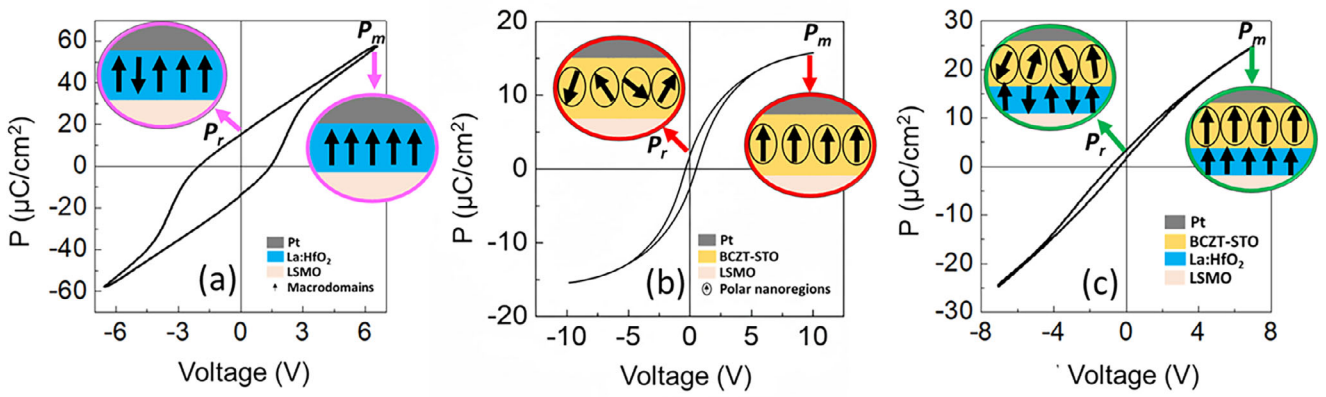

FIGURE 5 | Schematic illustration of the mechanism responsible for the observed *P-E* loops in (a) LSMO/La:HfO_2/Pt, (b) LSMO/BCZT-STO (200 nm) /Pt, and (c) LSMO/La:HfO_2/BCZT-STO (5 nm) /Pt capacitors. The insets show the dipole orientation corresponding to macrodomains and polar nanoregions in these capacitors.

La:HfO_2 [35, 37] and PNRs in BCZT-STO [24], as shown in the insets of Figure 5c. Thus, in this mixed FE/RFE system, the FE domains in La:HfO_2 can trigger the PNRs in RFE BCZT-STO, at low applied voltage [37]. Overall, the loop is narrower (less hysteretic) than for the LSMO/BCZT-STO/Pt (Figure S3b); (ESD = 2.6 J/cm^3 and η = 88%). Thus, η is high in the LSMO/La:HfO_2/BCZT-STO (5 nm)/Pt when compared to the one obtained in the LSMO/La:HfO_2/BCZT-STO/Pt, because the BCZT-STO layer is weakly polarized, induced by a lower voltage drop in the BCZT-STO layer. In RFE a higher voltage drop usually induces an higher hysteresis loss causing lower η [50]. The P_m value is intermediate between the LSMO/La:HfO_2/Pt and LSMO/BCZT-STO/Pt capacitors, as expected. The P_r value is significantly suppressed, since the randomly distributed PNRs, at zero voltage, can make the macrodomains in La:HfO_2 reduced in size, which thereby significantly decreases the P_r value. A minor imprint effect is also observed for the LSMO/La:HfO_2/BCZT-STO/Pt system as observed by the left-shifted hysteresis loop in Figure 5c. Interfacial effects from the presence of a built-in electric field can explain the origin of this imprint effect [38].

We now turn to understanding what is required for an effective energy harvesting-energy storage strategy for IoT devices. For this to be achieved, the ES device needs to efficiently release the stored energy. The capability of a dielectric capacitor to efficiently store a high ESD is quantitatively evaluated using the following equation [19]:

$$U_f = \frac{ESD}{1-\eta} \tag{7}$$

where U_f quantifies the extent to which ESD can be efficiently released. The U_f values for the STO/LSMO/La:HfO_2/BCZT-STO/Pt capacitors are found to be ~1016 J/cm^3 at 7.5 V, ~124 J/cm^3 at 8 V, ~375 J/cm^3 at 25 V, and ~183 J/cm^3 at 27 V, for the BCZT-STO layer thicknesses of 5, 50, 100, and 200 nm, respectively. The ES capacitor with a BCZT-STO layer thickness of 5 nm efficiently recovered a capacitive energy displaying an ultra-high value of U_f of 1016 J/cm^3 at just 7.5 V. Therefore, our FE/RFE heterostructure design and unique materials combination has together provided a novel way to undertake domain nanoengineering to achieve unprecedented dielectric energy storage properties.

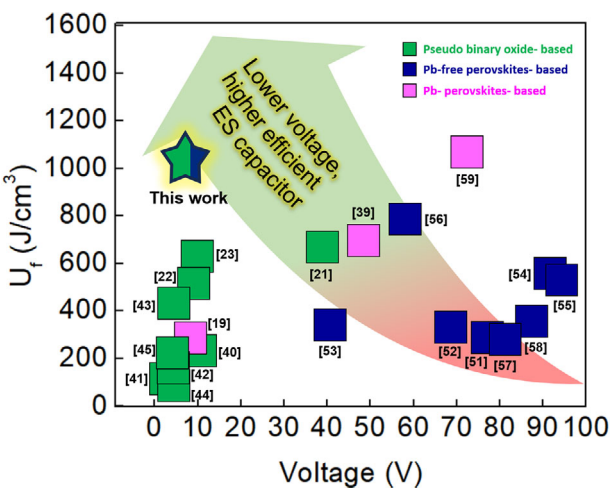

FIGURE 6 | Comparison of U_f as a function of voltages with the other reported best-performed works [19, 21–23, 39–45, 51–59]. The applied voltage corresponding to the best ES performance in the reported literature was estimated using the thickness and the breakdown voltage. The U_f values were also estimated, for the different works, by taking the energy storage density and efficiency of the capacitors.

Figure 6 displays the variation of U_f as a function of the applied voltage for the capacitors of this work compared to those reported in the literature for FE, AFE, and RFE systems [19, 21–23, 39–45, 51–59]. Our heterostructure concept had produced a record U_f value for a sub- 10 V applied voltage. Our design concept has therefore charted a new path for replacing the ES components in the low-voltage high-power microelectronic applications such as compact autonomous IoT sensor devices. Overall, we have developed a very promising dielectric alternative system to current state-of-the-art micro-batteries, electrochemical capacitors, and hybrid systems, which are limited in terms of high ESD and high η simultaneously.

4 | Conclusions

In this work, we propose and demonstrate a novel heterostructure thin film design approach to achieve unprecedented low-voltage

high energy storage density that can be efficiently released in a dielectric thin film capacitor. The heterostructure is composed on a layered film of a Pb-free ferroelectric (FE)-based material of La:HfO_2 and a relaxor ferroelectric (RFE) of BCZT-STO. The RFE layer thickness is carefully tuned to achieve effective voltages to optimize the respective functionalities of each layer. A high *ESD* of 51 J/cm^3 is achieved, and a very high η = 95%. These parameters enable an ultra-high U_f of 1016 J/cm^3 at a low operating voltage of 7.5 V. The remarkable performance results from the synergistic combination of the FE/RFE behavior in one single electrostatic capacitor, involving also a proximity effect that allows the switching of the BCZT-STO layer at lower applied voltages. Overall, the design enables a both a combination of the beneficial properties of each individual layer as well as a delicate trade-off of both *ESD* and η at low applied voltage. We have established a new materials design framework to overcome the high voltage requirement constraints associated with the current state of the art thin film electrostatic energy storage, allowing efficient energy storage for emerging electronic applications such as compact IoT sensors.

Acknowledgements

This work was supported by the Portuguese Foundation for Science and Technology (FCT) in the framework of the (i) Strategic Funding UID/04650/2025(DOI: https://doi.org/10.54499/UID/04650/2025), (ii) project 2024.12826.MIT (https://doi.org/10.54499/2024.12826.MIT), and (iii) project 2024.15998.PEX (https://doi.org/10.54499/2024.15998.PEX). J.P.B.S. also thanks FCT for the contract under the FCT Tenure program 1st edition. The authors would also like to thank engineer José Santos for the technical support at the Thin Film Laboratory. A.R.J. acknowledges the financial support by the short-term scientific mission (STSM) [Reference: E-COST-GRANT-CA20116-7127f89e] a grant of the European Cooperation in Science and Technology (COST) Action. Financial support from the Spanish Ministry of Science, Innovation and Universities (MCIN/AEI/ 10.13039/501100011033), through the Severo Ochoa MATRANS42 (CEX2023-001263-S), PDC2023-145874-I00, PID2023-147211OB-C21 and TED2021-130453B-C21 projects, from Generalitat de Catalunya (2021 SGR 00804). The authors acknowledge the assistance of the ICMAB-CSIC Scientific & Technical Services: Thin Films Laboratory (Raul Solanas and Victor Pardo) and X-ray Diffraction Laboratory (Anna Crespi, Joan Esquius and Francisco Javier Campos). MCI acknowledge funding from the Ministry of Education and Research through the Core Program of PNCDI 2022–2027, project No. PC3-PN23080303. The authors acknowledge the use of the Advanced Characterisation Facility at the Brunel Centre for Advanced Solidification Technology (BCAST), which was established with financial support from Research England UKRPIF 602. J.L. M.-D. acknowledges support from the Royal Academy of Engineering Chair in Emerging Technologies (Grant No. CiET1819\24), and the European Research Council ERC Advanced (Grant Agreement Nos. EU-H2020-ERC-ADG and 882929), EROS.

Open access publication funding provided by FCT (b-on).

Conflicts of Interest

The authors declare no conflicts of interest.

Data Availability Statement

The data that support the findings of this study are available from the corresponding author upon reasonable request.

References

1. V. Pecunia, L. G. Occhipinti, and R. L. Z. Hoye, "Emerging Indoor Photovoltaic Technologies for Sustainable Internet of Things," *Advanced Energy Materials* 11 (2021): 2100698, https://doi.org/10.1002/aenm.202100698.

2. A. Extance, "AI and the Rise of Intelligent Sensing," *Nature Sensors* 1 (2026): 3–6, https://doi.org/10.1038/s44460-025-00011-1.

3. S. Zhang, K. Zhao, T. Zhu, and J. Li, "Electrochemomechanical Degradation of High-capacity Battery Electrode Materials," *Progress in Materials Science* 89 (2017): 479–521, https://doi.org/10.1016/j.pmatsci.2017.04.014.

4. A. Manthiram, "An Outlook on Lithium Ion Battery Technology," *ACS Central Science* 3 (2017): 1063–1069, https://doi.org/10.1021/acscentsci.7b00288.

5. I. Arakistain, D. Zamora, D. Garcia-Sanchez, and A. Armijo, "LTO Battery Useful Life Prediction for Always on Edge aIoT Based Structural Health Monitoring," in The 26th European Conference on Power Electronics and Applications, (EPE Association, 2025), https://dx.doi.org/10.34746/epe2025-0264.

6. H. Ritchie, Does the World have Enough Lithium to Move to Electric Vehicles? published January 5, (2023), accessed: March 2030 https://www.sustainabilitybynumbers.com/p/lithium-electric-vehicles.

7. L. Liu, Y. Shang, A. Berbille, et al., "Self-powered Sensing Platform Based on Triboelectric Nanogenerators towards Intelligent Mining Industry," *Nature Communications* 16 (2025): 5141, https://doi.org/10.1038/s41467-025-60418-9.

8. S. Conti, "A Self-powered Integrated Fingertip-microgrid Sensing System," *Nature Reviews Electrical Engineering* 1 (2024): 637, https://doi.org/10.1038/s44287-024-00104-y.

9. N. Horiuchi, "Self-powered Sensors," *Nature Photonics* 12 (2018): 644, https://doi.org/10.1038/s41566-018-0290-5.

10. N. Meng, X. Ren, G. Santagiuliana, et al., "Ultrahigh β-phase Content Poly(vinylidene fluoride) with Relaxor-Like Ferroelectricity for High Energy Density Capacitors," *Nature Communications* 10 (2019): 4535, https://doi.org/10.1038/s41467-019-12391-3.

11. H. Palneedi, M. Peddigari, G. T. Hwang, D. Y. Jeong, and J. Ryu, "High-Performance Dielectric Ceramic Films for Energy Storage Capacitors: Progress and Outlook," *Advanced Functional Materials* 28 (2018): 1803665, https://doi.org/10.1002/adfm.201803665.

12. J. P. B. Silva, K. C. Sekhar, H. Pan, J. L. MacManus-Driscoll, and M. Pereira, "Advances in Dielectric Thin Films for Energy Storage Applications, Revealing the Promise of Group IV Binary Oxides," *ACS Energy Letters* 6 (2021): 2208–2217, https://doi.org/10.1021/acsenergylett.1c00313.

13. K. Yao, S. Chen, M. Rahimabady, et al., "Nonlinear Dielectric Thin Films for High-power Electric Storage with Energy Density Comparable with Electrochemical Supercapacitors," *IEEE Transactions on Ultrasonics, Ferroelectrics and Frequency Control* 58 (2011): 1968–1974, https://doi.org/10.1109/TUFFC.2011.2039.

14. A. R. Jayakrishnan, J. P. B. Silva, K. Kamakshi, et al., "Are Lead-free Relaxor Ferroelectric Materials the Most Promising Candidates for Energy Storage Capacitors?," *Progress in Materials Science* 132 (2023): 101046, https://doi.org/10.1016/j.pmatsci.2022.101046.

15. A. R. Jayakrishnan, B. Anina Anju, S. K. P. Nair, S. Dutta, and J. P. B. Silva, "Recent Development of Lead-free Relaxor Ferroelectric and Antiferroelectric Thin Films as Energy Storage Dielectric Capacitors," *Journal of the European Ceramic Society* 44 (2024): 4332, https://doi.org/10.1016/j.jeurceramsoc.2024.02.016.

16. B. Yang, Y. Liu, R.-J. Jiang, et al., "Enhanced Energy Storage in Antiferroelectrics via Antipolar Frustration," *Nature* 637 (2025): 1104–1110, https://doi.org/10.1038/s41586-024-08505-7.

17. H. Pan, S. Lan, S. Xu, et al., "Ultrahigh Energy Storage in Superparaelectric Relaxor Ferroelectrics," *Science* 374 (2021): 100.

18. Colby, "The Ultimate Guide to Selecting the Right Sensor for Your IoT PCB Design," All Electro Hub, https://www.allpcb.com/allelectrohub/the-ultimate-guide-to-selecting-the-right-sensor-for-your-iot-pcb-design, accessed September 19, 2025.

19. J. Belhadi, Z. Hanani, N. A. Shepelin, et al., "Ultra-high Energy Storage Density and Efficiency at Low Electric Fields/Voltages in Dielectric Thin Film Capacitors through Synergistic Effects," *Journal of Materiomics* 11 (2025): 100980, https://doi.org/10.1016/j.jmat.2024.100980.

20. A. R. Jayakrishnan, L. Marques, and J. P. B. Silva, *Ferroelectricity in Doped Hafnium Oxide*, 2nd Edition (Woodhead Publishing, 2025), 699–712, https://doi.org/10.1016/B978-0-443-29182-1.00040-0.

21. S. S. Cheema, N. Shanker, S.-L. Hsu, et al., "Giant Energy Storage and Power Density Negative Capacitance Superlattices," *Nature* 629 (2024): 803–809, https://doi.org/10.1038/s41586-024-07365-5.

22. W. Shuai, J. Y. Dai, Z. Xu, et al., "Superior and Ultrafast Energy Storage Performance of Relaxor Antiferroelectric HfO_2-based Supercapacitors," *Energy Storage Materials* 62 (2023): 102931, https://doi.org/10.1016/j.ensm.2023.102931.

23. J. Shin, D. H. Shin, H. Seo, et al., "Ultra-high Energy Storage Performance of Field-induced Ferroelectric Al_2O_3-inserted $Hf_{0.5}Zr_{0.5}O_2$ Thin Films for Electrostatic Supercapacitors," *Energy Storage Materials* 79 (2025): 104306, https://doi.org/10.1016/j.ensm.2025.104306.

24. R. J. M. Duarte, S. K. P. Nair, A. R. Jayakrishnan, et al., "Engineering Pb-free Relaxor Ferroelectric Thin Films for Low Voltage Energy Storage Applications," *Nanoscale* 17 (2025): 19794–19805, https://doi.org/10.1039/D5NR02537K.

25. T. Song, H. Tan, N. Dix, et al., "Stabilization of the Ferroelectric Phase in Epitaxial $Hf_{1-x}Zr_xO_2$ Enabling Coexistence of Ferroelectric and Enhanced Piezoelectric Properties," *ACS Applied Electronic Materials* 3 (2021): 2106–2113, https://doi.org/10.1021/acsaelm.1c00122.

26. T. Song, S. Estandía, I. Fina, and F. Sánchez, "Ferroelectric (Hf, Zr, La)O_2 Films," *Applied Materials Today* 29 (2022): 101661, https://doi.org/10.1016/j.apmt.2022.101661.

27. S. Starschich, D. Griesche, T. Schneller, R. Waser, and U. Böttger, "Chemical Solution Deposition of Ferroelectric Yttrium-doped Hafnium Oxide Films on Platinum Electrodes," *Applied Physics Letters* 104 (2014): 202903, https://doi.org/10.1063/1.4879283.

28. K. Chae, J. Hwang, E. Chagarov, A. Kummel, and K. Cho, "Stability of Ferroelectric and Antiferroelectric Hafnium–zirconium Oxide Thin Films," *Journal of Applied Physics* 128 (2020): 054101, https://doi.org/10.1063/5.0011547.

29. A. Silva, I. Fina, F. Sanchez, J. P. B. Silva, L. Marques, and V. Lenzi, "Unraveling the Ferroelectric Switching Mechanisms in Ferroelectric Pure and La Doped HfO_2 Epitaxial Thin Films," *Materials Today Physics* 34 (2023): 101064, https://doi.org/10.1016/j.mtphys.2023.101064.

30. M. G. Farahani, C. Magén, A. Quintana, I. Fina, and F. Sánchez, "Yttrium: A Highly Efficient Dopant for Ferroelectric HfO_2," *ACS Applied Electronic Materials* 7 (2025): 6628–6634.

31. I. Fina, L. Fàbrega, E. Langenberg, X. Martí, F. Sánchez, and M. Varela, "Nonferroelectric Contributions to the Hysteresis Cycles in Manganite Thin Films: a Comparative Study of Measurement Techniques," *Journal of Applied Physics* 109 (2011): 074105, https://doi.org/10.1063/1.3555098.

32. T. Song, R. Bachelet, G. Saint-Girons, N. Dix, I. Fina, and F. Sánchez, "Thickness Effect on the Ferroelectric Properties of La-doped HfO_2 Epitaxial Films Down to 4.5 Nm," *Journal of Materials Chemistry C* 9 (2021): 12224–12230, https://doi.org/10.1039/D1TC02512K.

33. A. R. Jayakrishnan, K. V. Alex, K. Kamakshi, J. P. B. Silva, K. C. Sekhar, and M. J. M. Gomes, *Journal of Materials Science: Materials in Electronics* 30 (2019): 19374–19382, https://doi.org/10.1007/s10854-019-02299-52019.

34. X. Lyu, F. Ali, T. Song, I. Fina, and F. Sánchez, "Cooperative Effects of Interface Symmetry, Redox Conditions and Low-thickness to Improve Polarization in Ferroelectric $Hf_{0.5}Zr_{0.5}O_2$ Films," *ACS Applied Materials & Interfaces* 17 (2025): 32596–32603, https://doi.org/10.1021/acsami.5c03527.

35. J. S. Kim, B. Gaggio, B. Bakhit, et al., "Reducing Coercive Field and Improving Endurance in Ferroelectric Epitaxial $Hf_{0.5}Zr_{0.5}O_2$ Thin Films via Novel Interface Layer Approach," *Advancement of Science* 13 (2025): 17314, https://doi.org/10.1002/advs.202517314.

36. J. Lyu, I. Fina, R. Solanas, J. Fontcuberta, and F. Sánchez, "Robust Ferroelectricity in Epitaxial $Hf_{1/2}Zr_{1/2}O_2$ Thin Films," *Applied Physics Letters* 113 (2018): 082902, https://doi.org/10.1063/1.5041715.

37. C. H. Skidmore, R. J. Spurling, J. Hayden, et al., "Proximity Ferroelectricity in Wurtzite Heterostructures," *Nature* 637 (2025): 574–579, https://doi.org/10.1038/s41586-024-08295-y.

38. M. D. Nguyen, E. P. Houwman, M. T. Do, and G. Rijnders, "Relaxor-ferroelectric Thin Film Heterostructure with Large Imprint for High Energy-storage Performance at Low Operating Voltage," *Energy Storage Materials* (2020): 25193–25201, https://doi.org/10.1016/j.ensm.2019.10.015.

39. M. D. Nguyen, Y. A. Birkhölzer, E. P. Houwman, G. Koster, and G. Rijnders, "Enhancing the Energy-Storage Density and Breakdown Strength in $PbZrO_3/Pb_{0.9}La_{0.1}Zr_{0.52}Ti_{0.48}O_3$-Derived Antiferroelectric/Relaxor-Ferroelectric Multilayers," *Advanced Energy Materials* 12 (2022): 2200517, https://doi.org/10.1002/aenm.202200517.

40. S. W. Lee, M. J. Jeong, Y. Oh, H. B. Kim, T. E. Park, and J. H. Ahn, "Enhanced Dielectric and Energy Storage Performances of $Hf_{0.6}Zr_{0.4}O_2$ Thin Films by Al Doping," *Ceramics International* 49 (2023): 18055–18060, https://doi.org/10.1016/j.ceramint.2023.02.173.

41. Y. Chen, Y. Yang, P. Yuan, et al., "Flexible $Hf_xZr_{1-x}O_2$ Thin Films on Polyimide for Energy Storage with High Flexibility," *IEEE Electron Device Letters* 43 (2022): 930–933, https://doi.org/10.1109/LED.2022.3171273.

42. D. Das, V. Gaddam, and S. Jeon, "Insertion of Dielectric Interlayer: a New Approach to Enhance Energy Storage in $Hf_xZr_{1-x}O_2$ Capacitors," *IEEE Electron Device Letters* 42 (2021): 331–334.

43. S. H. Yi, H. C. Lin, and M. J. Chen, "Ultra-high Energy Storage Density and Scale-up of Antiferroelectric $TiO_2/ZrO_2/TiO_2$ Stacks for Supercapacitors," *Journal of Materials Chemistry A* 9 (2021): 9081–9091, https://doi.org/10.1039/D0TA11991A.

44. M. Pešić, M. Hoffmann, C. Richter, T. Mikolajick, and U. Schroeder, "Nonvolatile Random Access Memory and Energy Storage Based on Antiferroelectric like Hysteresis in ZrO_2," *Advanced Functional Materials* 26 (2016): 7486–7494, https://doi.org/10.1002/adfm.201603182.

45. M. Hoffmann, U. Schroeder, C. Künneth, et al., "Ferroelectric Phase Transitions in Nanoscale HfO_2 Films Enable Giant Pyroelectric Energy Conversion and Highly Efficient Supercapacitors," *Nano Energy* 18 (2015): 154–164, https://doi.org/10.1016/j.nanoen.2015.10.005.

46. M. Si, X. Lyu, and P. D. Ye, "Ferroelectric Polarization Switching of Hafnium Zirconium Oxide in a Ferroelectric/Dielectric Stack," *ACS Applied Electronic Materials* 1 (2019): 745–751, https://doi.org/10.1021/acsaelm.9b00092.

47. T. Song, H. Tan, R. Bachelet, G. Saint-Girons, I. Fina, and F. Sánchez, "Impact of La Concentration on Ferroelectricity of La-doped HfO_2 Epitaxial Thin Films," *ACS Applied Electronic Materials* 3 (2021): 4809–4816, https://doi.org/10.1021/acsaelm.1c00672.

48. D. J. Appleby, N. K. Ponon, K. S. Kwa, et al., "Ferroelectric Properties in Thin Film Barium Titanate Grown Using Pulsed Laser Deposition," *Journal of Applied Physics* 116 (2014): 124105, https://doi.org/10.1063/1.4895050.

49. S. H. Park, J. Y. Kim, J. Y. Song, and H. W. Jang, "Overcoming Size Effects in Ferroelectric Thin Films," *Advanced Physics Research* 2 (2023): 2200096, https://doi.org/10.1002/apxr.202200096.

50. X. Zou, Z. Zhao, Y. Liu, Y. Lyu, S. Gao, and J. Luo, "Energy Storage Performance of BNT-based Relaxor Ferroelectric Thin Films by Introducing Highly Ergodic Components," *Ceramics International* (2025).

51. J. Qian, Z. Yu, G. Ge, et al., "Topological Vortex Domain Engineering for High Dielectric Energy Storage Performance," *Advanced Energy Materials* 14 (2024): 2303409, https://doi.org/10.1002/aenm.202303409.

52. Y. Liu, H. Han, H. Pan, S. Lan, Y. Lin, and J. Ma, "Enhancement of Breakdown Strength in Relaxor Ferroelectric $Ba(Zr_{0.3}Ti_{0.7})O_3$ Thin Film via Manipulating Growth Oxygen Pressure," *Journal of Alloys and Compounds* 937 (2023): 168452, https://doi.org/10.1016/j.jallcom.2022.168452.

53. H. Wang, H. Hao, D. Li, et al., "Synergistic Effect Enhances Energy Storage Properties of BNT-based Relaxor Ferroelectric Thin Films," *Ceramics International* 49 (2023): 12443–12451, https://doi.org/10.1016/j.ceramint.2022.12.104.

54. C. Bin, X. Hou, H. Yang, et al., "Flexible Lead-free Film Capacitor Based on $BiMg_{0.5}Ti_{0.5}O_3$-$SrTiO_3$ for High-performance Energy Storage," *Chemical Engineering Journal* 445 (2022): 136728, https://doi.org/10.1016/j.cej.2022.136728.

55. C. Bin, X. Hou, Y. Xie, et al., "Ultrahigh Energy Storage Performance of Flexible BMT-Based Thin Film Capacitors," *Small* 18 (2022): 2106209, https://doi.org/10.1002/smll.202106209.

56. A. Kursumovic, W. W. Li, S. Cho, P. J. Curran, D. H. L. Tjhe, and J. MacManus-Driscoll, "Lead-free Relaxor Thin Films with Huge Energy Density and Low Loss for High Temperature Applications," *Nano Energy* 71 (2020): 104536, https://doi.org/10.1016/j.nanoen.2020.104536.

57. P. Lv, C. Yang, J. Qian, et al., "Flexible Lead-Free Perovskite Oxide Multilayer Film Capacitor Based on $(Na_{0.8}K_{0.2})_{0.5}Bi_{0.5}TiO_3$/$Ba_{0.5}Sr_{0.5}(Ti_{0.97}Mn_{0.03})O_3$ for High-Performance Dielectric Energy Storage," *Advanced Energy Materials* 10 (2020): 1904229, https://doi.org/10.1002/aenm.201904229.

58. Z. Liang, M. Liu, L. Shen, et al., "All-inorganic Flexible Embedded Thin-film Capacitors for Dielectric Energy Storage with High Performance," *ACS Applied Materials & Interfaces* 11 (2019): 5247–5255, https://doi.org/10.1021/acsami.8b18429.

59. Y. Liu, Y. Zhang, J. Wang, et al., "Ultrahigh Capacitive Energy Storage through Dendritic Nanopolar Design," *Science* 388 (2025): 211–216, https://doi.org/10.1126/science.adt2703.

Supporting Information

Additional supporting information can be found online in the Supporting Information section.

Supporting File: adfm75213-sup-0001-SuppMat.docx.